

Cite this: *J. Mater. Chem. A*, 2016, 4, 3379

# A 'point–line–point' hybrid electrocatalyst for bi-functional catalysis of oxygen evolution and reduction reactions†

Hao-Fan Wang, Cheng Tang, Xiaolin Zhu and Qiang Zhang\*

Both oxygen evolution reaction (OER) and oxygen reduction reaction (ORR) hold the core position in various sustainable energy systems. Attributed to their sluggish kinetics, the principle and concept to achieve efficient electrocatalysts for a sustainable catalytic process, especially bi-functional electrocatalysts with abundant active centers and 3D conductive scaffolds for both OER and ORR, are strongly considered. In this contribution, rather than physically mixing active catalyst flakes with conductive fillers, a hybrid electrocatalyst with 'active point–conductive line–active point' connections was proposed and validated. As a proof-of-concept, Co-based active sites embedded on layered double oxide (LDO) substrates interlinked with carbon nanotubes (CNTs) were realized and exhibited a superior bi-functional activity for both OER and ORR in an alkaline electrolyte. The LDO/CNT hybrids catalyzed the OER to reach  $10.0 \text{ mA cm}^{-2}$  at  $1.64 \text{ V}$  vs. RHE, and the ORR to reach  $3.0 \text{ mA cm}^{-2}$  at  $0.65 \text{ V}$  vs. RHE, with a potential gap of  $0.99 \text{ V}$ . Such model catalysts of LDO/CNT hybrids even delivered a better bi-functional performance than routine noble metal catalysts (e.g. Pt/C and  $\text{IrO}_2$ ). The novel strategy of combining metal compounds and carbon nanomaterials through 'point–line–point' configurations can be applied to other hierarchical composites with multi-building blocks, aiming at promising applications in energy storage and environmental protection.

Received 17th November 2015  
Accepted 27th January 2016

DOI: 10.1039/c5ta09327a

[www.rsc.org/MaterialsA](http://www.rsc.org/MaterialsA)

## 1. Introduction

The decline of traditional fossil fuels has inspired the exploration of emerging energy resources and energy storage devices. Both oxygen evolution reaction (OER) and oxygen reduction reaction (ORR) are bottlenecks in a large amount of energy devices (e.g. fuel cells and metal–air batteries). Both OER and ORR suffer from sluggish kinetics and high overpotential. In order to achieve low energy consumption and promote the broad applications of these devices, an efficient bi-functional catalyst for the OER and ORR is urgently desired.

Precious metals and their oxides are acknowledged as effective OER or ORR catalysts,<sup>1</sup> but their bulk applications are limited by their high cost and limited natural abundance. Moreover, the bi-functional performance of precious metal catalysts is far from satisfactory. As an emerging research focus, transition metal (Ni, Fe, Co, Mn, *etc.*) compounds and doped carbon materials have been strongly considered as highly active electrocatalysts.<sup>2–13</sup> Among these precious-metal-free

electrocatalysts, cobalt compounds are notable for their superior bi-functional reactivity.<sup>14–21</sup> There are various valence states of cobalt species in these above-mentioned cobalt based catalysts that serve as OER and/or ORR active sites.<sup>18</sup> These non-precious-metal electrocatalysts have been integrated into metal–air batteries and fuel cells and demonstrated promising reactivity for the reversible ORR/OER.<sup>22–24</sup>

In respect of electrocatalysis, Co-based active sites were always small nanoparticles that were embedded onto a porous substrate to guarantee good dispersion and high exposure degree. However, cobalt oxides and hydroxides, as well as their substrates (e.g. MgO,  $\text{Al}_2\text{O}_3$ ,  $\text{TiO}_2$ ,  $\text{SiO}_2$ , layered double oxides (LDOs), and mixed oxides) possess very poor electrical conductivity. Therefore, carbon nanomaterials, featuring very high electrical conductivity and well-designed structures, were always introduced to render electron highways and achieve multi-functional nanostructures.

In most cases, metal based nanoparticles are always mixed with carbon nanomaterials (e.g. carbon black, graphene, and carbon nanotubes (CNTs)) for electrocatalysis.<sup>12,25–28</sup> However, a simple mixture of the two building blocks usually results in cluster–cluster connections (e.g. the typical 'line-face' contacts between catalyst flakes and 1D CNTs shown in Fig. 1a), resulting in poor contacts between the conductive agents and active centers. Consequently, a composite with cluster–cluster connections usually shows low electrical conductivity and poor

Beijing Key Laboratory of Green Chemical Reaction Engineering and Technology, Department of Chemical Engineering, Tsinghua University, Beijing 100084, PR China. E-mail: zhang-qiang@mails.tsinghua.edu.cn

† Electronic supplementary information (ESI) available: SEM images, XRD spectra of the hybrids, and a summary of the OER performances of transition metal compound-based composite catalysts. See DOI: 10.1039/c5ta09327a

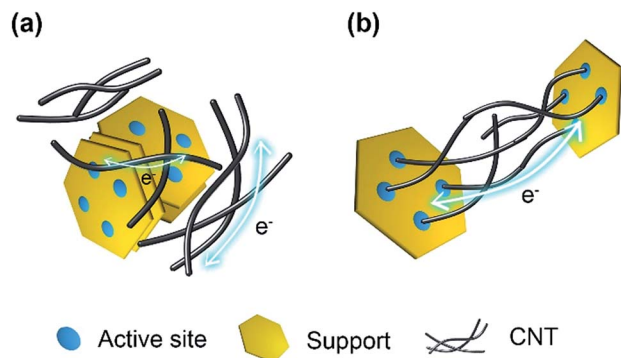


Fig. 1 The schematic diagram of the structures of (a) LDO + CNT mixture with 'line-face' contacts and (b) LDO/CNT hybrids with 'point-line-point' connections.

reactivity. The wise integration of Co-based catalysts and carbon nanomaterials is an important step to promote the activity of the composite catalyst.<sup>17,18</sup>

In this contribution, we proposed a novel composite catalyst with 'active point-conductive line-active point' configurations instead of routine electrocatalyst mixtures with 'cluster-cluster' contacts. Co-based nanoparticles were selected as the active centers and CNTs were employed as conductive lines. Co active sites were derived from the layered double hydroxides (LDHs) through facile calcination and reduction. The reason we select typical 2D anionic clays of LDHs is attributed to the fact that transitional metals can be dispersed *at an atomic level* with anticipated compositions. The LDOs obtained by facile calcination of LDHs were with mixed metal oxides or spinels as the main components. For instance, CoFeMgAl LDOs consisted of well-dispersed cobalt/iron oxides in high density on flake matrices, which were proved as highly efficient electrocatalysts for the OER and ORR.<sup>29-31</sup> As shown in Fig. 1a, both LDOs and CNTs aggregate into clusters in a mechanical mixture of LDOs and CNTs (denoted as LDO + CNT), leading to a LDO + CNT catalyst with 'line-face' connections. Many Co-based active sites are isolated in the LDO + CNT composite and do not contribute to the oxygen conversion in either ORR or OER. In contrast, if a 'point-line-point' configuration can be achieved, each active center is directly interlinked into 3D conductive scaffolds. Such 'point-line-point' configured LDO/CNT hybrids feature unique nanoparticle-nanoparticle (NP-NP) connections among LDOs and the *in situ* grown CNTs in this contribution. Every CNT is attached to a LDO flake, and implements a point-line-point combination with the Co-based active phase (Fig. 1b). Such a novel hierarchical LDO/CNT hybrid contributes to a superb bi-functional reactivity for both OER and ORR.

## 2. Results and discussion

### 2.1 Concept electrocatalyst of the 'point-line-point' configured LDO/CNT composite

Quaternary CoFeMgAl LDHs with a Co/Fe/Mg/Al molar ratio of 0.75 : 0.25 : 2 : 1 were first fabricated and then converted into LDOs under high temperature calcination. The scanning

electron microscopy (SEM) image of LDH flakes (Fig. S1†) exhibits a hexagonal structure with a lateral size of 600–800 nm. The as-obtained LDOs were then reduced by H<sub>2</sub> to generate metal nanoparticles for CNT growth.<sup>32,33</sup> The morphology of LDHs was well preserved (Fig. 2a). The Mg–Al spinel structure served as a substrate to maintain the original morphology of LDH flakes through the topological transformation during calcination. Both Co and Fe based active phases were uniformly distributed on the LDO flakes.<sup>32,34</sup> When a carbon source of C<sub>2</sub>H<sub>4</sub> was introduced at 700 °C, CNTs were *in situ* grown from the LDO flakes.<sup>35</sup> The nanostructure of the as-prepared LDO/CNT product was characterized by SEM (Fig. 2b). The stacked LDO flakes were propped apart by the *in situ* grown CNTs between them. A 3D electron pathway was achieved to facilitate the electrocatalytic reaction. The transmission electron microscopy (TEM) image of LDOs (Fig. 2c) reveals the formation of Kirkendall pores attributed to the diffusion of metal couples in the LDH precursors, which were preserved in LDO/CNT products (Fig. 2d). These mesopores on the LDO flakes are beneficial to gas transport during both OER and ORR. The connections between the CNTs and the active phases of LDOs

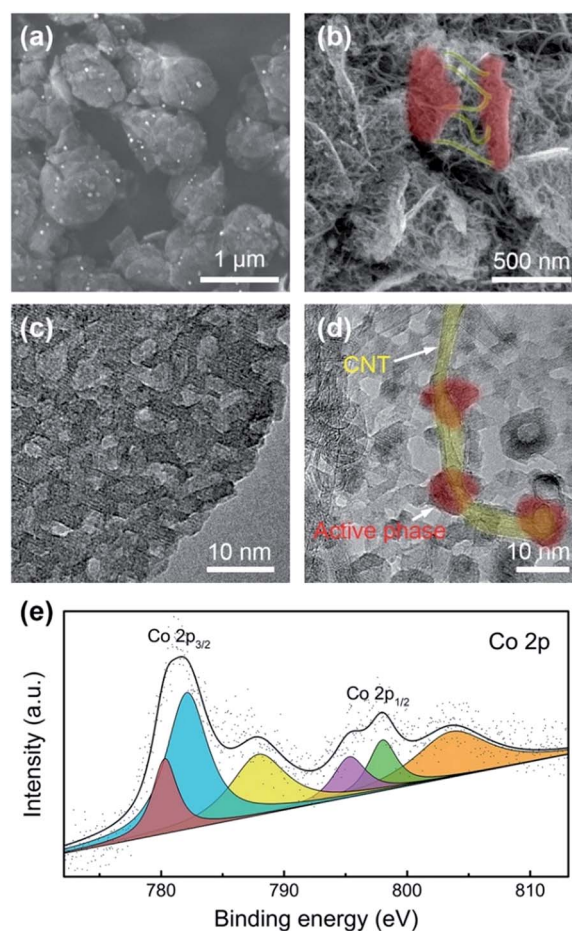


Fig. 2 Structural characterization of the LDO/CNT hybrids: the SEM images of (a) LDO and (b) LDO/CNT hybrids, the TEM images of (c) LDO and (d) LDO/CNT hybrids, and (e) the high resolution Co 2p spectra of LDO/CNT hybrids.

were also observed in Fig. 2d. The Co-containing active phases were separated apart by the insulating oxide substrates, which results in an inferior electrochemical performance. Attributed to the *in situ* CNT growth on LDOs, every individual CNT is attached to a metal nanoparticle embedded in LDO flakes, realizing an efficient NP–NP connection through a ‘point–line–point’ configuration. More direct evidence of this type of connection is observed in the low magnification TEM images of LDO/CNT hybrids (Fig. S2†). The CNTs interweave into 3D interconnected scaffolds with high electrical conductivity, thus interlinking the abundant active phases for electrocatalysis. While for the LDO + CNT mixture (Fig. S3†), the line–face interaction is not sufficient enough for CNTs to link up most of the active phases.

The X-ray diffraction (XRD) test was carried out (Fig. S4†) to probe the structure of LDO/CNT hybrids. The diffraction peaks are mainly indexed to the  $\text{MgAl}_2\text{O}_4$  spinel substrate (JCPDS no. 75-1796). The other components are amorphous or with very tiny size that they can't be confirmed by XRD characterization. To verify the chemical state of the cobalt in LDO/CNT hybrids, the X-ray photoelectron spectroscopy (XPS) pattern of Co 2p was collected (Fig. 2e). According to the published analysis of Co (2p) spectra of cobalt oxides,<sup>36</sup> the peaks at 780.3 and 782.1 eV are attributed to  $\text{Co}_{3/2}^{\text{III}}$  and  $\text{Co}_{3/2}^{\text{II}}$  configurations, respectively. The  $2p_{1/2}$  spin–orbit component appears at 795.3 and 798.0 eV for 3+ and 2+ Co species, respectively, and the peaks at 787.9 and 803.6 eV are  $\text{Co}^{2+}$  shake-up satellite peaks. It can be inferred that both  $\text{Co}^{2+}$  and  $\text{Co}^{3+}$  coexist in the LDO/CNT hybrids, with  $\text{Co}^{2+}$  in the majority. The activity of bivalent cobalt for OER and ORR catalysis is confirmed by previous published results,<sup>17,37</sup> attributed to the incorporation of Fe element into the LDO in this contribution, the as-obtained Co–Fe compound oxides both in LDO/CNT hybrids and the LDO + CNT mixture are expected to attain a better activity than the single cobalt oxide.<sup>31</sup> Additionally, the comparison of the Co 2p spectra of LDO, LDO + CNT and LDO/CNT indicates a strong interaction between LDO and CNT in LDO/CNT (Fig. S5†). The XPS spectra of LDO/CNT shows an obvious shift compared with LDO, while the peak position of LDO + CNT is nearly equal to that of LDO.

## 2.2 Electrocatalytic activity of ORR/OER

The electrochemical performance of LDO/CNT hybrids is presented in Fig. 3. LDOs before the carbon deposition, pure CNTs, and their mechanical mixture (LDO + CNT) were selected as control samples. All tests were performed in oxygen saturated 0.10 M KOH electrolyte using a three-electrode system. The catalysts were dispersed on the glassy carbon disk of a rotating ring-disk electrode (RRDE) with an areal loading amount of *ca.*  $0.25 \text{ mg cm}^{-2}$ .

The OER linear sweep voltammetry (LSV) plots at a scan rate of  $10.0 \text{ mV s}^{-1}$  are shown in Fig. 3a. LDO/CNT hybrids exhibit a lower OER onset potential than the individual LDO and CNT samples, while the onset potential of the LDO + CNT mixture is similar to that of the CNT electrocatalyst. This is attributed to direct chemical bonds between the CNTs and the active sites in the LDO/CNT hybrids. The potential required to achieve an OER current density of  $10.0 \text{ mA cm}^{-2}$  (denoted as  $E_{10}$ ) is a critical

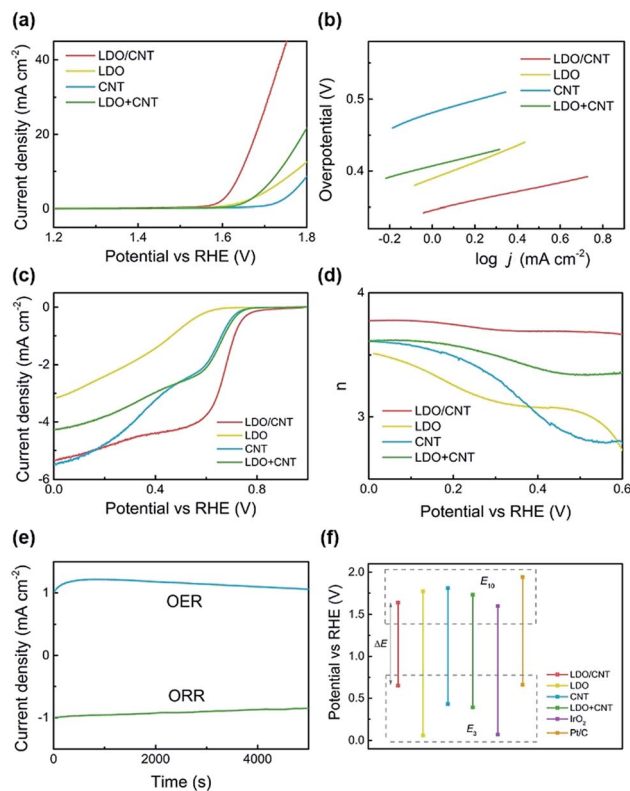


**Fig. 3** The electrocatalysis performance of the LDO/CNT hybrids. (a) The *i*–*R* compensated OER LSV curves at a scan rate of  $10.0 \text{ mV s}^{-1}$ . (b) Tafel plots. (c) ORR LSV curves at a scan rate of  $10.0 \text{ mV s}^{-1}$ . (d) The ORR electron transfer number calculated by the RRDE method. (e) Chronoamperometric response of LDO/CNT hybrids at an initial OER/ORR current density of  $1.0 \text{ mA cm}^{-2}$ . (f) Summary of  $E_{10}$ ,  $E_3$ , and  $\Delta E$  of all electrocatalysts in this contribution. All the tests were performed in  $\text{O}_2$ -saturated 0.10 M KOH solution, and the double layer capacitance current was removed in the LSV plots.

benchmark to evaluate the activity of the electrocatalyst.<sup>38</sup> The  $E_{10}$  of LDO/CNT hybrids is measured to be 1.65 V vs. RHE, which is much lower than 1.77 V for LDOs, 1.81 V for CNTs, and 1.73 V for the LDO + CNT mixture. The Tafel plots of the catalysts are presented in Fig. 3b. LDO/CNT hybrids also display a low Tafel slope of  $62 \text{ mV dec}^{-1}$ , while the Tafel slopes for LDO, CNT, and LDO + CNT electrocatalysts were 115, 92, and  $74 \text{ mV dec}^{-1}$ , respectively. The lower Tafel slope indicates a more favorable kinetics and a faster increase of the OER current density.

The LSV plots of the disk current for the ORR (Fig. 3c) confirm the superior ORR activity of LDO/CNT hybrids for the highest onset potential (*ca.* 0.84 V vs. RHE). The ORR electron transfer number was determined by the RRDE test (see details in the Experimental section in the ESI†). The results indicate that the ORR process catalyzed by LDO/CNT hybrids is closest to the 4-electron pathway, with the electron transfer number at around 3.8 (Fig. 3d). ORR tests with different rotating rates were also performed (Fig. S6†). The decrease of current density and electron transfer number with the decreasing rotating rate confirmed the mass transfer controlled feature of the ORR. Remarkably, the LDO/CNT catalyst also exhibited a good stability in long-time testing for both OER and ORR (Fig. 3e).

The bi-functional catalytic activity is evaluated by the potential gap ( $\Delta E$ ) between the potential required to achieve the  $3.0 \text{ mA cm}^{-2}$  OER current density ( $E_3$ ) and the potential required to achieve the  $10.0 \text{ mA cm}^{-2}$  OER current density ( $E_{10}$ ).<sup>14,18,25,39–41</sup> The comparison of  $E_{10}$ ,  $E_3$ , and  $\Delta E$  of each catalyst is presented in Fig. 3f, and also listed in Table S1.† The LDO/CNT hybrids exhibit the best bi-functional reactivity with the lowest  $\Delta E$  of 0.99 V, while the  $\Delta E$  values of LDOs and CNTs are much higher (1.71 and 1.38 V, respectively), and the mechanical LDO + CNT mixture also delivers an inferior  $\Delta E$  (1.34 V) in contrast with the LDO/CNT electrocatalyst. The bi-functional performance of noble metal catalysts  $\text{IrO}_2$  and Pt/C for the OER and ORR was also tested (Fig. S7†). The measured  $\Delta E$  turned out to be 1.53 V for  $\text{IrO}_2$  and 1.28 V for Pt/C. The noble metal catalysts are highly active for one of the reactions (OER or ORR), while usually not favourable for the other reaction. Consequently, the LDO/CNT hybrid with ‘point–line–point’ connections affords a remarkable activity for both OER and ORR. This is more promising for related energy devices such as metal–air batteries and reversible fuel cells.

### 2.3 The role of ‘point–line–point’ hybrids

The *in situ* grown LDO/CNT hybrids with high intrinsic activities and well-designed nanostructures are identified as a superb bi-functional electrocatalyst for both OER and ORR. In respect of the active material, the bi-functional activity of LDO/CNT hybrids is mainly contributed by the cobalt species in LDO. After the calcination of LDHs, the cobalt hydroxides convert into Co oxides and Co-based spinel oxides.<sup>42–44</sup> Both Co oxides and Co-based spinels are recognized as efficient electrocatalysts,<sup>2,19,28,44,45</sup> leading to an improved electrocatalytic performance (Fig. S8†). Moreover, the Fe in LDOs is acknowledged as a key component to enhance the OER activity.<sup>3,46,47</sup> The Fe compounds display low Tafel slopes in the OER process,<sup>46</sup> implying an improved kinetics. The rational incorporation of the Fe and Co oxides introduces an OER catalyst with highly active sites, and the ORR activity of Co–Fe oxides was also verified in previous publications.<sup>29,30</sup> Fig. S9† exhibits the OER and ORR LSV plots of CoFeMgAl LDO/CNT hybrids (*i.e.* LDO/CNT hybrids in this contribution) and CoMgAl LDO/CNT hybrids. Both the low onset potential and high current density of CoFeMgAl LDO/CNT hybrids indicate the important role of Fe synergy for extraordinary reactivity in the OER and ORR.

Additionally, the LDO flakes with abundant mesopores serve as thin substrates to disperse and anchor both Co and Fe active sites into a hierarchical electrocatalyst (Fig. 2d). Those mesopores enlarge the exposed surface area of LDOs, and directly serve as the transport channels for the gas phase. This significantly accelerates the gas-involved reactions of both OER and ORR. During the CVD growth of CNTs,  $\text{H}_2$  was introduced into the tube furnace to facilitate the formation of the CNT catalyst. Meanwhile, the  $\text{H}_2$  reduction can also induce the surface amorphization of the oxides.<sup>48</sup> The amorphous surface of LDOs is decorated with hydrated species and possesses a larger specific surface area, and thus is expected to deliver a better electrochemical performance than the crystalline surface.<sup>31,48</sup>

However, the activity of LDOs was still far from satisfactory, due to the separated active phases scattered on the insulated Mg–Al oxide substrate and consequently limited electron pathways.

Consequently, the point–line–point connections between CNTs and the active phases are necessary configurations to link the separated active sites and fully demonstrate the superb reactivity, which is supported by the electrochemically active surface area (ECSA) measurements. Fig. 4a and b exhibit the double-layer capacity ( $C_{dl}$ ) test results of the LDO/CNT samples. The  $C_{dl}$  was measured by cyclic voltammetry (CV) in a potential range without pseudo-reactions (Fig. 4a). The difference of the charging current density and the discharging current density,  $\Delta j$ , is a linear function of the CV scan rate (Fig. 4b), and the slope is twice  $C_{dl}$ , which is proportional to the ECSA.<sup>38</sup> Due to the stackable layered structure of LDOs, this material possesses an extremely low ECSA. In the mechanical mixture of LDOs and CNTs, the ‘line–face’ contacts at the cluster level are difficult to link all active sites, resulting in a partial segregation of active sites without electron pathways and therefore a limited ECSA. In terms of LDO/CNT hybrids, attributed to the ‘point–line–point’ connections, the active phases were fully exposed and inter-linked with each other by the highly conductive CNTs. The efficient exposure of the active phases in LDO/CNT hybrids can be unambiguously confirmed by the significant improvement of the ECSA compared with that of the LDO + CNT mixture.

Furthermore, the interfacial transfer plays an important role in the electrocatalysis. To further investigate the effect on the charge transfer resistance and electrical conductivity by the *in*

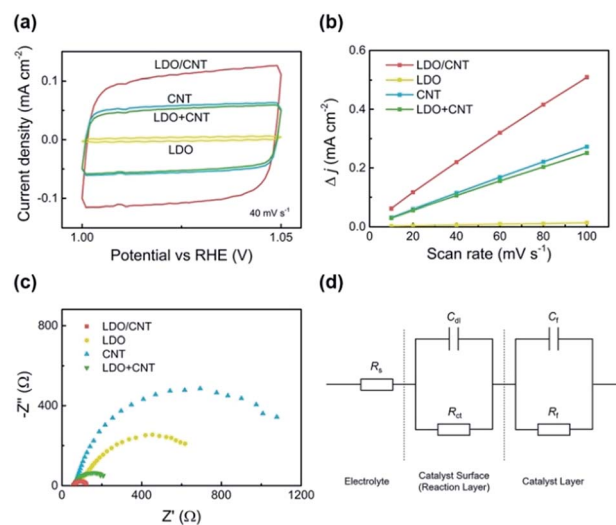


Fig. 4 The electrochemical test of LDO/CNT hybrids and LDO + CNT mixtures. (a) The CV curves at a scan rate of  $40 \text{ mV s}^{-1}$ . (b) Charging current density differences plotted against scan rates. The linear slope, equivalent to twice the double-layer capacitance  $C_{dl}$ , was employed to represent the ECSA. (c) Nyquist plots obtained from EIS measurements at a potential of 1.66 V vs. RHE. The electrochemical measurements were performed in  $\text{O}_2$ -saturated 0.10 M KOH solution. (d) Equivalent circuit used to fit the impedance data in (c).  $R_s$  is the resistance of the electrolyte.  $C_{dl}$  is the double layer capacitance and  $R_{ct}$  is the charge transfer resistance.  $R_f$  is the resistance of the catalysts layer and  $C_f$  is the capacitance.<sup>49</sup>

*situ* CNT growth and the 'point-line-point' connection, an AC impedance test was carried out. The electrochemical impedance spectroscopy (EIS) was performed at 1.66 V vs. RHE in a frequency range of 0.1–10<sup>5</sup> Hz with an amplitude of 5.0 mV (Fig. 4c). The equivalent circuit (Fig. 4d) is divided into three parts: the electrolyte, the catalyst surface where the reaction takes place, and the catalyst layer.<sup>49,50</sup> The fitting results are listed in Table 1. The charge transfer resistance ( $R_{ct}$ ) for LDO/CNT hybrids is the lowest, and the  $R_{ct}$  for LDOs is similar to that of LDO/CNT hybrids, indicating the Co-based LDOs with hydrophilic interfaces as an efficient active material for the surface reaction, which is consistent with other reports.<sup>21,38</sup> In addition, the high  $R_{ct}$  of hydrophobic CNTs corresponds to the low activity. The resistance of the catalyst layer ( $R_f$ ) represents the electrical conductivity of the electrocatalyst. After incorporation with CNTs, the resistance of LDOs is significantly decreased. Due to the covalent bonding between CNTs and excellent contacts among CNTs in LDO/CNT hybrids, the  $R_f$  is further reduced. By comparing the  $R_{ct}$  and  $R_f$  of LDO/CNT hybrids and the LDO + CNT mixture, it is concluded that the hybrids with 'point-line-point' connections possess the advantages from both components through the rational integration of the electrochemically active sites on LDOs and the highly conductive CNTs. Such 'point-line-point' connections play a critical role in integrating LDOs and CNTs, thus facilitating the interfacial charge transfer and electron transport in the 3D nanostructured hybrids. Besides, the quantitative relationship of the double layer capacitance of each sample measured by EIS agrees well with the CV results in Fig. 4a and b.

From the above discussion, the superb bi-functional LDO/CNT hybrids for the ORR/OER are attributed to the ubiquitous 'point-line-point' connections between CNTs and LDOs. The Co/Fe sites provide high intrinsic bi-functional activity; CNTs constitute the electrically conductive framework; the 'point-line-point' connections of active sites and CNTs bring out the best utilization of CNTs in strengthening the electron transfer. As demonstrated by the EIS test, both the charge transfer and the electron transport resistance are significantly reduced through the 'point-line-point' connections. Since the CNTs are *in situ* grown on the LDO flakes, almost every CNT building block is directly connected with active nanoparticles embedded on LDO flakes. As a result, every CNT is available to transfer the electrons between the active phases and the glassy carbon electrode during the electrocatalysis process. In this way, the surface reaction on LDOs is also accelerated, rendering a very high activity for both OER and ORR. In contrast, the mechanical

mixture of LDOs and CNTs with 'line-face' connections results in an insufficient utilization of both components. Additionally, the *in situ* grown CNTs can also separate the stacked LDOs and enlarge the surface area, thus realizing the adequate exposure of the active phases.

### 3. Conclusions

The Co-based LDOs were well combined with CNTs into 'point-line-point' configured LDO/CNT hybrids with an extraordinary bi-functional reactivity for both ORR and OER. The LDO/CNT catalyst exhibited a low OER–ORR potential gap of 0.99 V, which is much smaller than those of the routine noble metal catalysts (IrO<sub>2</sub>, and Pt/C) and a mixture of LDOs and CNTs. The rational structure design strategy to enhance the contact of catalyst components and improve the utilization efficiency of the active phases is instructive for future investigation on advanced electrocatalysts. Such a general strategy is expected to inspire novel material chemistry and 3D nanostructures through rational hybridization of active sites and conductive scaffolds with interlinked electron highways, high-density exposed active sites, and interconnected ion/reactant/product diffusion channels.

### 4. Experimental section

#### 4.1 *In situ* CVD hybridization of the LDO/CNT electrocatalyst

The LDHs were synthesized by a co-precipitation method in an oil bath. To a solution of 10.0 mmol Mg(NO<sub>3</sub>)<sub>2</sub>·6H<sub>2</sub>O, 5.0 mmol Al(NO<sub>3</sub>)<sub>3</sub>·9H<sub>2</sub>O, 3.75 mmol Co(NO<sub>3</sub>)<sub>2</sub>·6H<sub>2</sub>O, 1.25 mmol Fe(NO<sub>3</sub>)<sub>3</sub>·9H<sub>2</sub>O (the mole ratio of Co : Fe : Mg : Al = 0.75 : 0.25 : 2 : 1), and 0.60 mol urea, 200 mL deionized water was decanted into a 500 mL round-bottom flask. Then the flask was heated at 100 °C in an oil bath with magnetic stirring for 12.0 h, followed by 12.0 h standing at 94 °C. The product was vacuum filtered and washed with deionized water. After 24 h freeze drying of the filter cake, the LDHs were obtained. The CNTs were grown by the CVD method. About 0.15 g of LDHs was dispersed uniformly on a quartz boat which was placed in the center of a horizontal quartz tube at atmospheric pressure. The tube was then inserted into a furnace. Under flowing Ar (200 mL min<sup>-1</sup>), the reactor was heated to 700 °C, and then H<sub>2</sub> (20 mL min<sup>-1</sup>) was introduced into the reactor for 1.0 min for reduction. After that, the C<sub>2</sub>H<sub>4</sub> was introduced at a flow rate of 50 mL min<sup>-1</sup> for another 5.0 min for the catalytic growth of CNTs. Afterwards, the furnace was cooled to room temperature under Ar protection. The LDO/CNT hybrids were obtained and collected. The LDOs were prepared in a similar way to that of LDO/CNT hybrids, except that C<sub>2</sub>H<sub>4</sub> was not introduced into the furnace at 700 °C.

The LDO + CNT mixture was prepared by mixing the as-prepared LDOs and CNTs using a mortar. The CNTs were grown on LDOs and then the catalyst was removed. The mass ratio of LDOs and CNTs was the same as that of LDO/CNT hybrids. The CNT content in LDO/CNT hybrids was obtained by thermogravimetric analysis (TGA, Fig. S10<sup>†</sup>) in an O<sub>2</sub> atmosphere, and the amount was measured to be 59.5 wt%. Due to the ultrasonic

**Table 1** The fitted resistance and capacitance parameters corresponding to the EIS spectra

Samples	$R_s$ ( $\Omega$ )	$R_{ct}$ ( $\Omega$ )	$C_{dl}$ ( $\mu\text{F cm}^{-2}$ )	$R_f$ ( $\Omega$ )	$C_f$ ( $\mu\text{F cm}^{-2}$ )
LDO/CNT	57.6	50.1	4933	11.5	1323
LDO	60.4	57.9	50.6	505	599
CNT	59.0	986	1649	29.8	1125
LDO + CNT	60.5	132	1649	21.3	843

treatment in the process of working electrode fabrication, the LDOs and CNTs can be regarded as well mixed.

## 4.2 Structural characterization

The morphology of the electrocatalysts was characterized using a JSM 7401F SEM operating at 3.0 kV and a JEM 2010 high-resolution TEM operating at 120.0 kV. The carbon deposition amount of CNTs on LDO/CNT hybrids and was obtained through a TGA method by using a TGA/DSC1 STAR<sup>c</sup> system under an N<sub>2</sub> flow. XRD patterns were recorded on a Bruker D8 Advance diffractometer at 40.0 kV and 120 mA with Cu-K $\alpha$  radiation. The XPS measurements were carried out by using an Escalab 250Xi.

## 4.3 Electrocatalytic performance evaluation

Electrochemical measurements were performed on a RRDE (Pine Research Instrument, USA) in a three-electrode electrochemical setup using a computer-controlled electrochemistry workstation (CHI 760D, CH Instrument, USA). A platinum sheet electrode and a saturated calomel electrode (SCE) served as the counter and reference electrodes, respectively. The reference electrode has been calibrated with the standard hydrogen electrode. The rotating ring-disk electrode with a disk diameter of 5.0 mm served as the substrate for the working electrode.

The working electrode was fabricated by the drop casting method. 5.0 mg of the catalyst was dispersed in 0.95 mL of ethanol and 0.05 mL of 5.0 wt% Nafion solution by about 1.0 h sonication to form a relatively homogeneous suspension. Then 10  $\mu$ L of the catalyst suspension was transferred onto the glass carbon disk electrode (0.196 cm<sup>2</sup>) *via* a controlled drop casting approach. The electrode was then dried in air. After the solvent evaporation, the catalyst clung to the GC electrode of the RDE or RRDE to serve as the working electrode.

The measurements were carried out in O<sub>2</sub>-saturated 0.10 M KOH solution, and the RRDE was rotated at 1600 rpm. Before other measurements were performed, the catalyst was cycled several times by CV. OER and ORR activities were tested by LSV at a scan rate of 10 mV s<sup>-1</sup>. 95% *iR*-compensation was applied during LSV tests. The data of the Tafel slope were transformed from the LSV plots. During the ORR LSV test, the Pt ring electrode was set at a constant potential of 0.50 V *vs.* SCE to detect the peroxide intermediates. The electron transfer number *n* was calculated based on the disk and ring current as follows:

$$n = \frac{4I_d}{I_d + I_r/N}$$

where *I<sub>d</sub>* is the disk current, *I<sub>r</sub>* is the ring current, and *N* is the current collection efficiency of the Pt ring which was determined to be 0.26.

The electrochemically active surface area (ECSA) was determined by measuring the capacitive current associated with double-layer charging from the scan-rate dependence of CV. This measurement was performed on the same working electrodes in a potential window of 1.00–1.05 V *vs.* RHE and scan rates ranging from 10 to 100 mV s<sup>-1</sup>. Then linear fitting of the charging current density differences ( $\Delta j = j_a - j_c$  at a potential of

1.025 V *vs.* RHE) against the scan rate was done. The slope is twice the double-layer capacitance *C<sub>dl</sub>*, which is used to represent ECSA.

The EIS test was carried out on the working electrodes at an anodic polarization potential of 0.65 V *vs.* SCE (1.66 V *vs.* RHE). The spectra were collected in a frequency range of 0.1–10<sup>5</sup> Hz with an amplitude of 5.0 mV.

The potential *vs.* RHE (*E vs.* RHE) was calculated by the following equation: *E vs.* RHE = *E vs.* SCE + 0.059 pH + 0.24 (*E vs.* SCE stands for the potential *vs.* SCE) and the overpotential  $\eta = E$  *vs.* RHE – 1.23.

## Acknowledgements

This work was financially supported by the National Natural Science Foundation of China (No. 21306102 and 21422604) and the Tsinghua University Initiative Scientific Research Program (2014z22076). We also acknowledge the helpful discussion from Dr Gui-Li Tian, Bo-Quan Li, and Jia-Le Shi.

## Notes and references

- 1 T. C. Wen and C. C. Hu, *J. Electrochem. Soc.*, 1992, **139**, 2158.
- 2 J. Bao, X. Zhang, B. Fan, J. Zhang, M. Zhou, W. Yang, X. Hu, H. Wang, B. Pan and Y. Xie, *Angew. Chem., Int. Ed.*, 2015, **54**, 7399.
- 3 M. S. Burke, M. G. Kast, L. Trotochaud, A. M. Smith and S. W. Boettcher, *J. Am. Chem. Soc.*, 2015, **137**, 3638.
- 4 J. Wang, K. Wang, F.-B. Wang and X.-H. Xia, *Nat. Commun.*, 2014, **5**, 5285.
- 5 Y. Jiao, Y. Zheng, M. T. Jaroniec and S. Z. Qiao, *Chem. Soc. Rev.*, 2015, **44**, 2060.
- 6 Z. Lu, Y. Li, X. Lei, J. Liu and X. Sun, *Mater. Horiz.*, 2015, **2**, 294.
- 7 D. S. Yu, K. L. Goh, L. Wei, H. Wang, Q. Zhang, W. C. Jiang, R. M. Si and Y. Chen, *J. Mater. Chem. A*, 2013, **1**, 11061.
- 8 R. J. White, N. Brun, V. L. Budarin, J. H. Clark and M. M. Titirici, *ChemSusChem*, 2014, **7**, 670.
- 9 F. Song and X. Hu, *J. Am. Chem. Soc.*, 2014, **136**, 16481.
- 10 H.-F. Wang, C. Tang and Q. Zhang, *J. Mater. Chem. A*, 2015, **3**, 16183.
- 11 X. Zhu, C. Tang, H.-F. Wang, Q. Zhang, C. Yang and F. Wei, *J. Mater. Chem. A*, 2015, **3**, 24540.
- 12 C. Tang, H. S. Wang, H. F. Wang, Q. Zhang, G. L. Tian, J. Q. Nie and F. Wei, *Adv. Mater.*, 2015, **27**, 4516.
- 13 R. Chen, G. Sun, C. Yang, L. Zhang, J. Miao, H. B. Tao, H. Yang, J. Chen, P. Chen and B. Liu, *Nanoscale Horizons*, 2016, **1**, DOI: 10.1039/c5nh00082c.
- 14 Y. Zhan, G. Du, S. Yang, C. Xu, M. Lu, Z. Liu and J. Y. Lee, *ACS Appl. Mater. Interfaces*, 2015, **7**, 12930.
- 15 X. Li, Y. Fang, X. Lin, M. Tian, X. An, Y. Fu, R. Li, J. Jin and J. Ma, *J. Mater. Chem. A*, 2015, **3**, 17392.
- 16 T. Y. Ma, S. Dai, M. Jaroniec and S. Z. Qiao, *J. Am. Chem. Soc.*, 2014, **136**, 13925.
- 17 S. Mao, Z. Wen, T. Huang, Y. Hou and J. Chen, *Energy Environ. Sci.*, 2014, **7**, 609.

- 18 Y. Wang, W. Ding, S. Chen, Y. Nie, K. Xiong and Z. Wei, *Chem. Commun.*, 2014, **50**, 15529.
- 19 M. Hamdani, R. N. Singh and P. Chartier, *Int. J. Electrochem. Sci.*, 2010, **5**, 556.
- 20 G. L. Tian, M. Q. Zhao, D. S. Yu, X. Y. Kong, J. Q. Huang, Q. Zhang and F. Wei, *Small*, 2014, **10**, 2251.
- 21 L. Qian, Z. Y. Lu, T. H. Xu, X. C. Wu, Y. Tian, Y. P. Li, Z. Y. Huo, X. M. Sun and X. Duan, *Adv. Energy Mater.*, 2015, **5**, 1500245.
- 22 J. H. Kim, A. G. Kannan, H. S. Woo, D. G. Jin, W. Kim, K. Ryu and D. W. Kim, *J. Mater. Chem. A*, 2015, **3**, 18456.
- 23 X. Liu, M. Park, M. G. Kim, S. Gupta, G. Wu and J. Cho, *Angew. Chem., Int. Ed.*, 2015, **54**, 9654.
- 24 J. T. Zhang, Z. H. Zhao, Z. H. Xia and L. M. Dai, *Nat. Nanotechnol.*, 2015, **10**, 444.
- 25 K. Xie, J. Masa, E. Madej, F. Yang, P. Weide, W. Dong, M. Muhler, W. Schuhmann and W. Xia, *ChemCatChem*, 2015, **7**, 3027.
- 26 Z. Wang, S. Xiao, Z. Zhu, X. Long, X. Zheng, X. Lu and S. Yang, *ACS Appl. Mater. Interfaces*, 2015, **7**, 4048.
- 27 S. Liu, L. Li, H. S. Ahn and A. Manthiram, *J. Mater. Chem. A*, 2015, **3**, 11615.
- 28 Y. Hou, Z. H. Wen, S. M. Cui, S. Q. Ci, S. Mao and J. H. Chen, *Adv. Funct. Mater.*, 2015, **25**, 872.
- 29 W. Yan, Z. Yang, W. Bian and R. Yang, *Carbon*, 2015, **92**, 74.
- 30 W. Bian, Z. Yang, P. Strasser and R. Yang, *J. Power Sources*, 2014, **250**, 196.
- 31 A. Indra, P. W. Menezes, N. R. Sahraie, A. Bergmann, C. Das, M. Tallarida, D. Schmeißer, P. Strasser and M. Driess, *J. Am. Chem. Soc.*, 2014, **136**, 17530.
- 32 G.-L. Tian, M.-Q. Zhao, B. Zhang, Q. Zhang, W. Zhang, J.-Q. Huang, T.-C. Chen, W.-Z. Qian, D. S. Su and F. Wei, *J. Mater. Chem. A*, 2014, **2**, 1686.
- 33 C. M. Li, M. Wei, D. G. Evans and X. Duan, *Small*, 2014, **10**, 4469.
- 34 M. Q. Zhao, Q. Zhang, J. Q. Huang and F. Wei, *Adv. Funct. Mater.*, 2012, **22**, 675.
- 35 M. Q. Zhao, Q. Zhang, X. L. Jia, J. Q. Huang, Y. H. Zhang and F. Wei, *Adv. Funct. Mater.*, 2010, **20**, 677.
- 36 L. Fu, Z. Liu, Y. Liu, B. Han, P. Hu, L. Cao and D. Zhu, *Adv. Mater.*, 2005, **17**, 217.
- 37 L. Wang, C. Lin, D. Huang, F. Zhang, M. Wang and J. Jin, *ACS Appl. Mater. Interfaces*, 2014, **6**, 10172.
- 38 C. C. L. McCrory, S. Jung, J. C. Peters and T. F. Jaramillo, *J. Am. Chem. Soc.*, 2013, **135**, 16977.
- 39 Y. Zhao, K. Kamiya, K. Hashimoto and S. Nakanishi, *J. Phys. Chem. C*, 2015, **119**, 2583.
- 40 Y. Gorlin and T. F. Jaramillo, *J. Am. Chem. Soc.*, 2010, **132**, 13612.
- 41 T. Y. Ma, J. Ran, S. Dai, M. Jaroniec and S. Z. Qiao, *Angew. Chem., Int. Ed.*, 2015, **54**, 4646.
- 42 M.-Q. Zhao, Q. Zhang, J.-Q. Huang, G.-L. Tian, T.-C. Chen, W.-Z. Qian and F. Wei, *Carbon*, 2013, **54**, 403.
- 43 D. C. Carvalho, N. A. Ferreira, J. M. Filho, O. P. Ferreira, J. M. Soares and A. C. Oliveira, *Catal. Today*, 2015, **250**, 155.
- 44 H. Hu, B. Guan, B. Xia and X. W. Lou, *J. Am. Chem. Soc.*, 2015, **137**, 5590.
- 45 R. Chen, H.-Y. Wang, J. Miao, H. Yang and B. Liu, *Nano Energy*, 2015, **11**, 333.
- 46 M. S. Burke, S. Zou, L. J. Enman, J. E. Kellon, C. A. Gabor, E. Pledger and S. W. Boettcher, *J. Phys. Chem. Lett.*, 2015, **6**, 3737.
- 47 Z. Li, M. Shao, H. An, Z. Wang, S. Xu, M. Wei, D. G. Evans and X. Duan, *Chem. Sci.*, 2015, **6**, 6624.
- 48 X. Leng, Q. Zeng, K.-H. Wu, I. R. Gentle and D.-W. Wang, *RSC Adv.*, 2015, **5**, 27823.
- 49 Y. Meng, W. Song, H. Huang, Z. Ren, S. Y. Chen and S. L. Suib, *J. Am. Chem. Soc.*, 2014, **136**, 11452.
- 50 R. L. Doyle and M. E. Lyons, *Phys. Chem. Chem. Phys.*, 2013, **15**, 5224.